geosciences

MDPI

Article

The Application of Horizontal Directional Drilling for the Geological Investigation of Super-Long Tunnels: A Case Study

Qiang Zhao [1], Xuefeng Yan [2], Jiguo Liu [1,*], Sheng Huang [3] and Baosong Ma [3]

[1] CCCC Second Highway Consultants Co., Ltd., Wuhan 430056, China; zhaoq226@mail.sysu.edu.cn
[2] Faculty of Engineering, China University of Geosciences, Wuhan 430074, China
[3] School of Civil Engineering, Sun Yat-sen University, Guangzhou 510275, China; mabaoso@mail.sysu.edu.cn (B.M.)
* Correspondence: liujiguogg@163.com

Abstract

With the increasing construction of ultra-long tunnels, complex and highly variable geological conditions along tunnel alignments pose major challenges to geological investigation, design, and construction. Conventional vertical drilling mainly provides discrete vertical geological profiles and is limited in its ability to continuously characterize lithological variations, fracture zones, and groundwater conditions along the tunnel axis. To overcome this limitation, this study proposes an integrated investigation approach based on horizontal directional drilling (HDD) for continuous along-axis geological exploration. Using the Tianshan Shengli Tunnel as the geological setting, the technical advantages of HDD for tunnel investigation—including ultra-long reach, ultra-high accuracy, high penetration rate, and strong adaptability—are first summarized. An integrated investigation method is then developed by combining HDD with targeted borehole coring, hydraulic fracturing, comprehensive borehole logging, and borehole TV imaging. A 2271 m long investigation borehole was drilled along the tunnel axis from the portal section. As a result, precise directional control limited the maximum deviation between the HDD borehole trajectory and the tunnel axis to only 6.32 m. Meanwhile, the lag distance between cuttings was determined through theoretical calculations to reconstruct the true borehole positions corresponding to the collected cuttings. Based on XRD mineralogical analysis, macroscopic observations, and preliminary investigation results, the lithology of the tunnel surrounding rock was delineated with high resolution. In addition, daily borehole inflow was monitored, and tunnel inflow during construction was predicted using the groundwater dynamics method and an empirical railway relationship, yielding an expected normal inflow of 4016.6 m^3/d and a maximum inflow of 12,049.8 m^3/d; furthermore, borehole TV footage was used to accurately locate inflow points and intervals with well-developed joints and fractures within the surrounding rock. Highlights This study proposes an HDD–downhole geophysics method for tunnel investigation, classifies surrounding-rock lithology from cuttings and cores, and predicts tunnel construction inflow from HDD borehole inflow monitoring data.

Keywords: horizontal directional drilling; super-long tunnel geological investigation; borehole coring; borehole TV; tunnel water inflow prediction

Check for updates

Academic Editor: Hongyuan Liu

Received: 8 March 2026
Revised: 18 June 2026
Accepted: 25 June 2026
Published: 7 July 2026

Copyright: © 2026 by the authors. Licensee MDPI, Basel, Switzerland. This article is an open access article distributed under the terms and conditions of the Creative Commons Attribution (CC BY) license.

1. Introduction

The construction of super-long tunnels at high altitudes, in mountainous terrain, or offshore poses substantial challenges for geological investigation, design, and construc-

tion. Although conventional vertical drilling is a mature technique and can characterize vertical geological conditions with relatively high accuracy, it is less effective for geological exploration along the tunnel alignment and often lacks the resolution needed to accurately represent the surrounding rock's geological characteristics. Therefore, there is an urgent need to develop new concepts and methods for the geological investigation of super-long, deep-buried tunnels in complex environments.

Horizontal directional drilling (HDD) is a technology primarily used for trenchless pipeline construction [1,2]. In recent years, however, an increasing number of researchers have advocated extending HDD to tunnel geological investigation. Between 1964 and 1981, Japan first applied small-diameter HDD in the Seikan Tunnel and completed 105 boreholes; nevertheless, no corresponding downhole testing results were reported [3]. Considering the extreme topographic conditions of the Sichuan–Tibet Railway corridor—high elevation, rugged terrain, large relief, and limited accessibility—Zhang et al. [4] developed a detailed 3000 m HDD exploration scheme, including drilling equipment and construction procedures, to obtain more comprehensive physical–geological evidence while reducing the drilling workload. When discussing the challenges and key technological breakthroughs associated with large, long tunnels, Chen [5] and Yan [6] also proposed integrating HDD with downhole geophysical methods for the geological exploration of major long tunnels. Shu et al. [7] further elaborated on the technical advantages, necessity, and feasibility of applying HDD to tunnel geological investigation. In the Shiziyang main navigation channel project in the Guangdong–Hong Kong–Macao Greater Bay Area, Wang et al. [8] employed an integrated approach combining multi-target HDD, horizontal coring using a positive displacement motor (PDM), and memory drill-pipe-conveyed logging to characterize lithology, rock-mass integrity, and permeability for a 934 m subsea tunnel, thereby enabling accurate geological prediction along the channel.

Compared with Liu [9], which primarily focused on predicting tunnel groundwater inflow using HDD borehole inflow monitoring and Goodman back-calculation of permeability, the present study treats groundwater prediction as only one component of a broader HDD-based geological investigation framework. Compared with Wang et al. [8], which demonstrated multi-target HDD, horizontal coring, and drill-pipe-conveyed logging in a 934 m subsea tunnel, this study emphasizes continuous along-axis characterization in a 2271 m mountain tunnel borehole. The new contributions include trajectory representativeness analysis, cutting-lag correction, XRD-assisted lithological classification of transported cuttings, local core verification, borehole-TV-based localization of water-entry points and fracture-rich intervals, and integrated interpretation of lithology, fractures, and groundwater conditions along the tunnel axis.

Overall, previous tunnel HDD studies have demonstrated the feasibility of long-distance directional exploration, horizontal coring, downhole logging, and groundwater-inflow prediction. However, continuous geological characterization directly along the tunnel axis remains insufficiently verified. In particular, the true in situ depths of transported cuttings cannot be determined without considering the lag distance caused by mud circulation. In addition, the integrated use of lag-corrected cuttings, mineralogical analysis, core verification, borehole inflow monitoring, and borehole TV imaging still requires further field validation in super-long mountain tunnels. Therefore, this study uses the Tianshan Shengli Tunnel as a case study to evaluate an integrated HDD-based investigation workflow. Specifically, this study aims to evaluate the trajectory-control performance and spatial representativeness of a 2271 m tunnel axis HDD borehole, correct the actual depths of cuttings, refine lithological classification using XRD and macroscopic observations, predict tunnel water inflow from borehole inflow monitoring data, and identify water-entry points and fracture-rich intervals using borehole TV imaging.

2. Technical Advantages of HDD in Tunnel Geological Investigation Technology

HDD technology offers distinct advantages over traditional vertical drilling techniques. This technology exhibits exceptional features, including ultra-long reach, ultra-high accuracy, high penetration rate, and strong adaptability. These unique attributes make HDD a superior choice for geological investigation in tunnel construction projects.

2.1. Ultra-Long Reach

Long-distance capability is an important prerequisite for applying HDD to tunnel geological investigation. However, this capability should be evaluated using tunnel investigation boreholes rather than pipeline-crossing projects, because geological investigation boreholes require trajectory control, geological sampling, borehole stability, logging access, and data quality assurance [10]. Previous tunnel-related studies have shown the potential of HDD for long-distance geological exploration. For example, small-diameter horizontal boreholes were used in the Seikan Tunnel, and HDD-based investigation schemes have also been proposed or applied in long tunnel projects. Wang et al. [8] reported a 934 m HDD borehole for the Shiziyang subsea tunnel, combining horizontal coring and logging. In the present study, a 2271 m HDD borehole was drilled along the tunnel axis of the Tianshan Shengli Tunnel, providing a field-scale example of long-distance HDD-based geological investigation in a super-long mountain tunnel.

2.2. Trajectory-Control and Geological Investigation Accuracy

The accuracy of HDD technology for tunnel geological investigation comprises two aspects: trajectory-control accuracy and geological investigation accuracy. Trajectory-control accuracy refers to the ability to guide the borehole along the designed tunnel alignment. Geological investigation accuracy refers to the reliability of geological information derived from cuttings, cores, borehole logging, borehole TV imaging, and water-inflow monitoring. Compared with conventional vertical drilling, HDD can provide more continuous geological information along the tunnel axis. However, the trajectory of an HDD borehole may still locally deviate from the tunnel excavation envelope, especially when magnetic/geomagnetic guidance is affected by metallic interference in the tunnel environment [11,12].

2.2.1. Directional Control

The measurement-while-drilling (MWD) system used in HDD technology comprises both wired and wireless guidance systems. However, wireless steering technology is affected by drilling depth, so wired steering technology is more commonly used in super-long-distance steering drilling. The wired guidance technology consists of two main components: the bottom-hole system and the ground system. The bottom-hole system includes non-magnetic drill collars, sondes, centralizers, and non-magnetic extension rods. On the other hand, the ground system includes control-signal transmission cables, data-receiving converters, data-processing computers, and drillers' monitors (Figure 1).

During guided drilling, the operator uses the wired magnetic field control system to measure the drilling tool's depth, dip angle, azimuth, and tool face angle. Based on these measurements, the operator adjusts the drilling tool's azimuth to ensure the pilot hole is drilled accurately along the desired trajectory [13–17].

In this project, a P2 guidance system (P2, USA) was used for trajectory control. The guidance accuracy may be affected by metallic materials in the tunnel environment, such as reinforcement bars in the tunnel lining, steel ribs, rock bolts, wire mesh, pipelines, and nearby construction equipment [18]. These materials can disturb the local magnetic

field and reduce the reliability of azimuth measurements, leading to trajectory deviations. Therefore, the trajectory-control performance should be evaluated based on the measured spatial relationship between the borehole trajectory and the tunnel excavation envelope.

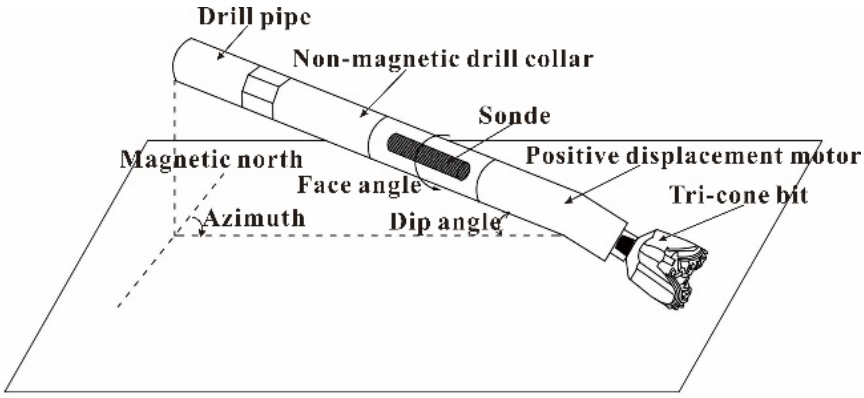


Figure 1. Structural representation of HDD guided drilling tool assembly.

2.2.2. The Accuracy of Geological Investigation

The accuracy of geological investigation is reflected in HDD's ability to obtain continuous, multi-source geological information along the tunnel alignment. Cuttings and cores can be used for lithological identification and mineralogical analysis. Comprehensive borehole logging can provide geophysical responses related to lithology and rock-mass integrity. Borehole TV imaging can directly identify borehole-wall conditions, fractures, broken zones, and water-entry points. Therefore, although local trajectory deviations may affect the direct spatial representativeness of some intervals, the integrated use of cuttings, cores, logging, borehole TV, and inflow monitoring can improve the reliability of geological interpretation along the tunnel axis.

2.3. High Penetration Rate

When HDD adopts a tri-cone bit for the whole Section Broken Drilling in the rock mass, the penetration rate can reach 151 m/d. Figure 2 shows the single-day footage in the Tianshan Shengli Tunnel HDD Geological Investigation Project.

Figure 2 shows that in the Tianshan Shengli Tunnel HDD Geological Investigation Project, the drilling speed exceeded 100 m/d for 9 d, with a maximum of 151 m/d.

2.4. Strong Adaptability

As shown in Figure 3a, conventional vertical drilling is a mature technique with well-established standards and can provide a clear, intuitive depiction of the rock mass's vertical geological conditions. However, it is less accurate for investigating geology along a horizontal alignment, particularly for tunnel surrounding-rock investigations under complex stratigraphic conditions [19,20]. In contrast, HDD can be used to explore the surrounding rock along the tunnel alignment by positioning the HDD rig at relatively flexible locations, such as the tunnel portal, cross passages within the tunnel, or the side of the mountain (Figure 3b). With a directional control system, the investigation borehole can be steered to advance accurately along the tunnel axis, thereby effectively compensating for the limitations of conventional vertical drilling.

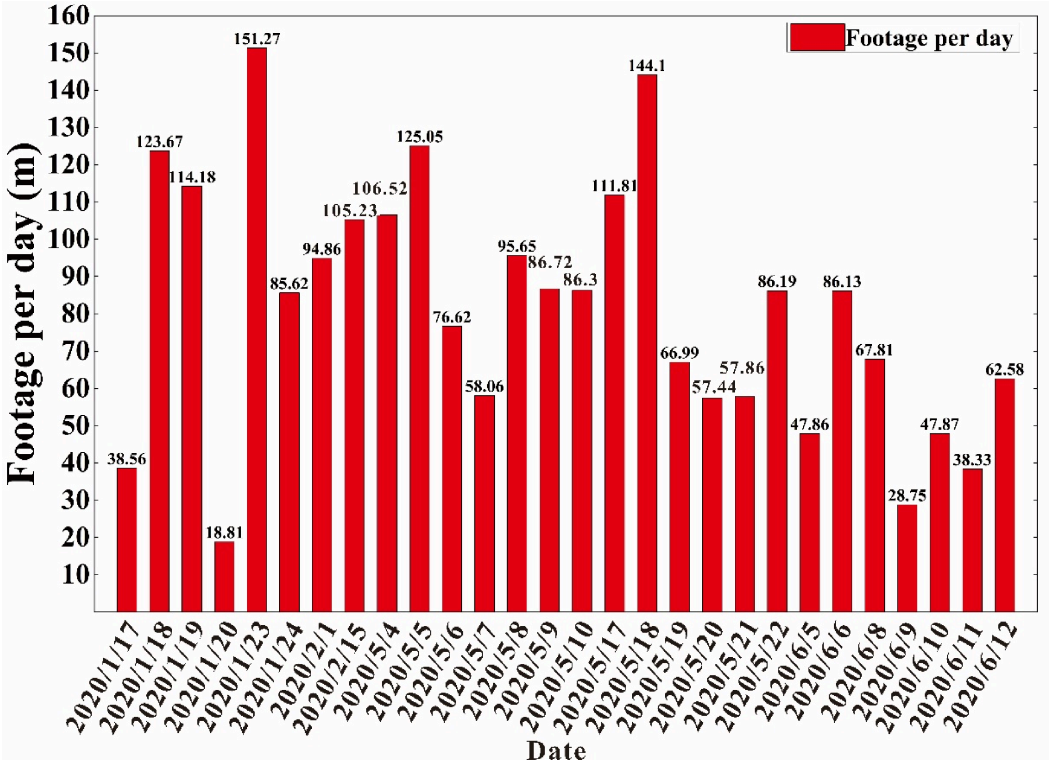


Figure 2. HDD single-day footage histogram of Tianshan Shengli Tunnel.

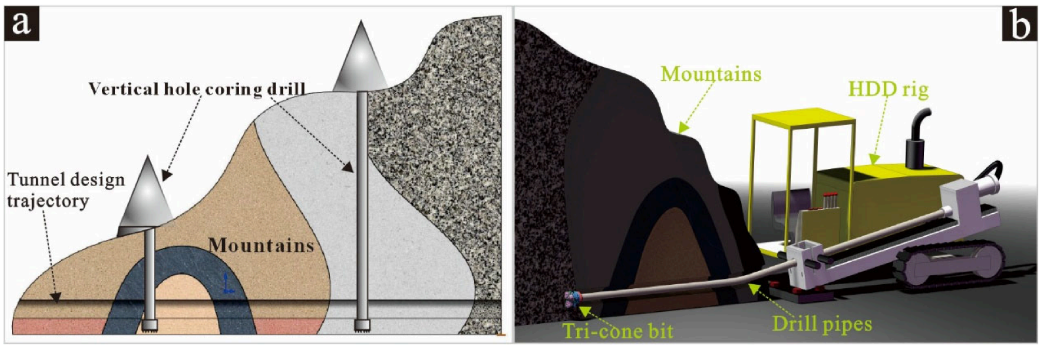


Figure 3. Comparison between conventional vertical drilling and HDD-based tunnel geological investigation. (**a**) Conventional vertical borehole coring; (**b**) HDD-based geological investigation along the tunnel axis.

3. Project Overview and Investigation Methods

3.1. Geological and Hydrogeological Setting of the Project

The Tianshan Shengli Tunnel is located in northwestern China, with a total length of 22.0 km and a maximum overburden depth of approximately 1200 m. The tunnel crosses a complex mountain geological setting characterized by large topographic relief, variable lithology, and active tectonic structures. According to previous geological mapping and preliminary investigation data, the main lithologies along the HDD investigation section include tuffaceous sandstone, granodiorite, carbonaceous slate, quartz schist, and gneissic granite. The Borokonu–Achik Kuduk fault zone, located about 1900 m from the tunnel portal, is a long-term active fault and a critical structure controlling rock-mass integrity, fracture development, and groundwater conditions. The geological setting, tunnel alignment, fault zone, and planned HDD trajectory are shown in Figure 4.

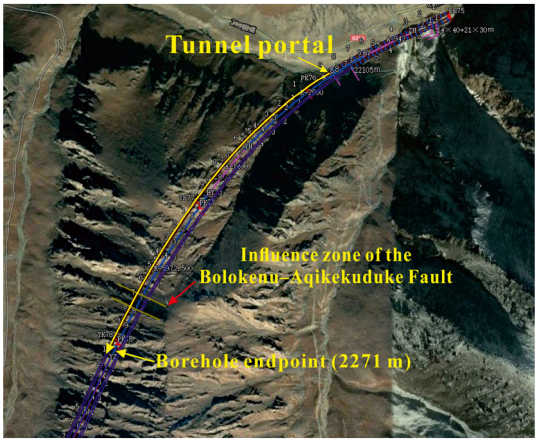


Figure 4. Satellite image showing the HDD investigation borehole trajectory, tunnel alignment, and the influence zone of the Bolokenu Aqikekuduke fault. The blue line indicates the tunnel alignment, the red lines indicate the influence zone of the Bolokenu Aqikekuduke fault, and the yellow line indicates the HDD investigation borehole trajectory.

Hydrogeologically, groundwater in the tunnel area mainly consists of loose-deposit pore water, weathered bedrock fracture water, and tectonic fracture water. The surface-water system is mainly composed of the Urumqi River, Wulastai River, and Alagou River. The Urumqi River is recharged by glacier meltwater, snowmelt, rainfall, and groundwater, with a mean annual runoff of approximately 2.44×10^8 m^3, about 79% of which occurs from June to September. The surface-water flow in nearby gullies and tributaries ranges from about 0.065 to 7.37 m^3/s, and some gully floors are hundreds of meters higher than the tunnel elevation, providing favorable recharge conditions. Therefore, groundwater occurrence is highly heterogeneous and is mainly controlled by topography, lithology, fault/fracture development, intrusive contacts, and fracture-rich zones [21,22]. For tunnel inflow prediction, the hydraulic head H represents the effective groundwater head rather than the tunnel overburden thickness, and was determined from previous hydrogeological data, borehole water-level observations, and local topographic conditions.

Given the tunnel's long alignment, high elevation, large overburden, complex lithological variation, and locally developed water-bearing fracture zones, conventional vertical drilling alone is insufficient to provide continuous geological information along the tunnel axis. Therefore, HDD was adopted to drill from the tunnel portal toward the fault zone along the tunnel axis, as illustrated in Figure 4. During drilling, cutting collection, local coring, borehole inflow monitoring, and borehole TV imaging were conducted to obtain continuous geological and hydrogeological information on the surrounding rock.

3.2. HDD System

The construction equipment used for the HDD-based geological investigation of the Tianshan Shengli Tunnel comprises an HDD rig, drill pipes, a guiding device, mud pumps, generators, mud tanks, a vibrating screen, a mud pool, and a water reservoir. During construction, water is pumped from the reservoir into the mud tanks, where it is mixed with bentonite and polymer additives to prepare drilling mud. The mud is then pumped by the mud pump into the drill string of the HDD rig. As the tri-cone bit advances, the mud transports cuttings from the bottom of the borehole to the returns slurry pool at the borehole outlet. The mud returns containing cuttings are screened through the vibrating screen and discharged into the mud pool. Finally, the mud in the pit is pumped back into the mud tanks for recirculation and reuse. Figure 5 presents the plan view of the on-site construction equipment layout.

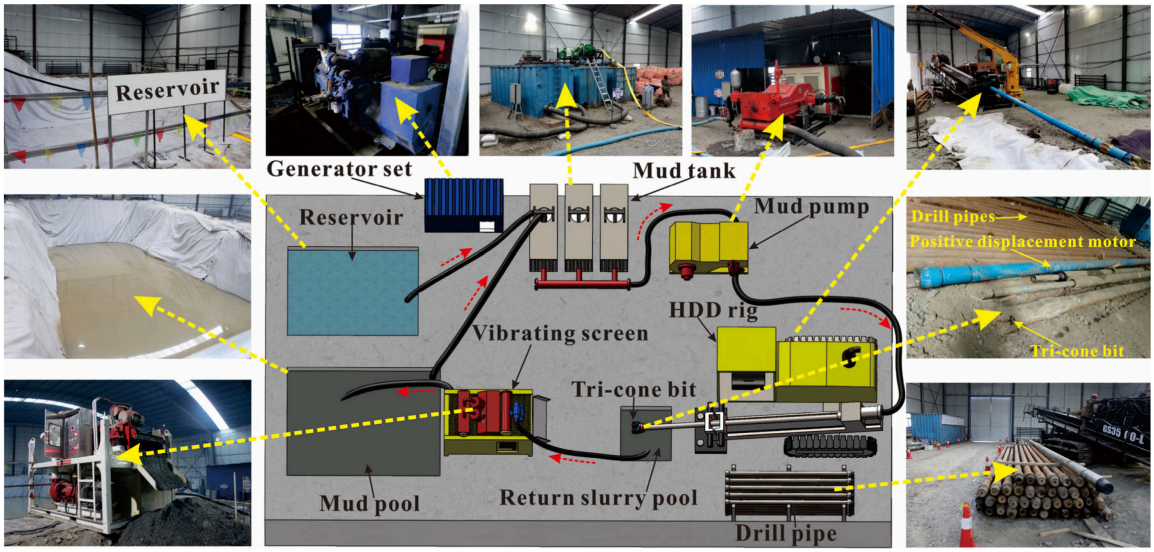


Figure 5. On-site layout of the HDD equipment used for tunnel geological investigation. The red arrows indicate the mud circulation process, and the yellow dashed arrows indicate the correspondence between the field photographs and the schematic components.

In this project, the GD3500-L HDD rig (Jiangsu Goodeng Engineering Machinery Equipment Co., Ltd., Yancheng, China) provides a maximum push/pull force of 3580 kN; detailed specifications are listed in Table 1. The QZNB-2500 mud pump (Hengyang Zhongdi Equipment Prospecting Engineering Machinery Co., Ltd., Hengyang, China) delivers a maximum flow rate of 2270 L/min and a maximum mud pressure of 10 MPa; detailed specifications are given in Table 2. The positive displacement motor (PDM) (Aoruituo Energy Technology Co., Ltd., Wuhu, China) has a maximum torque of 16,323 N·m; detailed specifications are presented in Table 3.

Table 1. GD3500-L rig specifications.

Item	Parameter
Overall dimensions (main unit)	17,900 × 3440 × 3300 mm
Main unit mass	45 t
Engine power	264 × 2 kW
Rated hydraulic system working pressure	35 MPa
Maximum output torque of the power head	112,000 N·m
Maximum pull force of the power head	3580 kN
Maximum push/pull speed of the power head	45 m/min
Drill pipe diameter × length	Φ168/Φ140 × 9600 mm
Maximum mud pressure	20 MPa
Maximum crawler travel speed	2.5 km/h

Table 2. The technical specifications of the QZNB-2500 mud pump.

Item	Parameter	Item	Parameter
Pump input power	300 kW	Displacement per revolution	20.52 L/r
Stroke length	180 mm	Rated pump speed	120 spm
Gearbox reduction ratio	3.321:1	Maximum flow rate	2270 L/min
Cylinder bore	Φ220	Maximum pressure	10 MPa

Table 3. The technical parameters of the PDM.

Item	Parameter	Item	Parameter
Screw specifications	7LZ-172-5.6	Maximum torque	16,323 N·m
Number of threads	7/8	Motor pressure drop	6 MPa
Bearing section length	788 mm	Displacement per revolution	13 L/r
Hydraulic axial force	188.11 kN	Recommended flow rate	1200–2400 L/min
Rated torque	11,659 N·m	Bit speed	92–185 rpm

3.3. Scheme Design of HDD Used in Tunnel Geological Investigation

The tunnel geological investigation using HDD technology involves several sequential steps. First, a pilot hole is drilled along the tunnel design axis from the portal section using a tri-cone bit to achieve full-face rock-breaking. During drilling, cuttings are collected in real time, and the water inflow rate is monitored daily. Upon reaching the designated coring interval, the drilling assembly is retrieved and replaced with a coring assembly to initiate coring operations. After coring is completed, an in situ hydraulic fracturing test can be conducted at the coring interval. Subsequently, the coring assembly is replaced with the tri-cone bit to resume full-face rock-breaking drilling, and drilling continues until the target depth is reached. After completion of the borehole, the drill string is withdrawn, and in situ investigations—including comprehensive borehole logging and borehole TV imaging—are performed along the entire borehole. To improve methodological reproducibility, key drilling and testing information was recorded throughout the investigation, including measured depth, drill-pipe number, sampling time, rate of penetration, mud flow rate, mud pressure, and any abnormal events. The borehole trajectory and measured depth were checked against the drilling records before coring, interpretation of cuttings, inflow monitoring, and borehole TV imaging. The detailed construction workflow is illustrated in Figure 6.

3.3.1. Coring and Collection of Rock Cuttings

The coring and collection of rock cuttings included the following two procedures:

(1) Coring. In the HDD borehole, intermittent coring was carried out using a diamond coring drill, as shown in Figure 7. The core position in the borehole can be set in the mutation section, softer lithologic section, and critical point of the fault zone of tunnel construction. Before coring, the target interval was selected based on the designed depth, trajectory record, and drilling response. After retrieval, core length, recovery rate, RQD, photographs, and lithological descriptions were recorded on site. The procedure for HDD coring involves several steps. When the tri-cone drill bit reaches the designed position, the DTA is fully withdrawn. The diamond coring drill and single-action-double-pipe drilling tool are then installed and pushed to the coring position for the coring operation. After coring, all the drilling tools are pulled out. This operation is repeated until all the coring work is completed.

(2) Collection of rock cuttings. As shown in Figure 8a,b, during drilling, a 100-mesh sieve with an aperture size of 0.15 mm was used at the borehole collar to collect the returning cuttings. The cuttings were collected at a fixed drilling advance interval of 10 m, and each sample was bagged immediately after collection. This fixed-interval sampling strategy was adopted to ensure the continuity and representativeness of the cutting samples along the borehole. The depth and sample ID were recorded on each bag (Figure 8c). Each cutting sample was assigned a unique ID, and the corresponding depth, sampling time, and drill-pipe number were recorded. The sieve was cleaned before sampling to reduce cross-contamination. The recorded collection depth was later corrected using the calculated cutting-lag distance. After completion of the cutting collection, the samples were subjected

to XRD analysis and macroscopic characterization. Before XRD analysis, visible drilling-mud coatings and soft residues on the cuttings were removed as far as possible to reduce the potential influence of bentonite and polymer additives. Finally, a vibrating sieve was used to determine the particle-size distribution of the cuttings (Figure 8d).

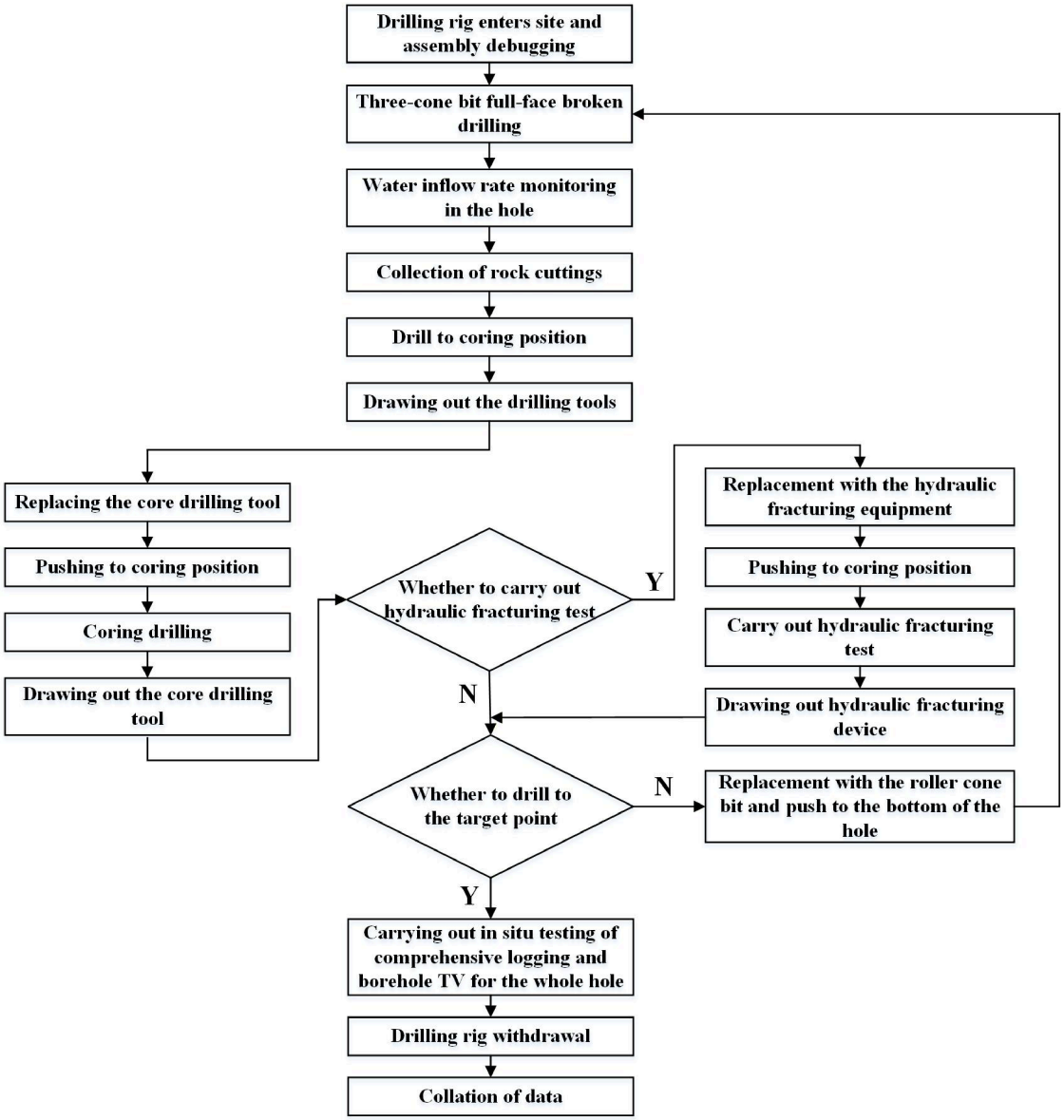


Figure 6. Scheme design of HDD technology for tunnel geological investigation.

3.3.2. Borehole TV Test Scheme

Upon completion of the final hole, all drilling tools are removed from the borehole, and a battery storage borehole TV device, as shown in Figure 9, is inserted in their place. The device is then switched on from the orifice, and the horizontal directional drill rods are slowly used to push it into the bottom of the hole before pulling it back to the orifice. The investigation focuses on the lithology of the surrounding rock of the borehole, the development status of joint fissures, and the influence range of the fractured fault zone [23]. During the detection process, it is essential to avoid injecting slurry and to prevent the drill rods from rotating. During the borehole TV test, the probe was slowly pushed and pulled to maintain image clarity, and video was continuously recorded throughout the test. Fractures, broken rock-mass zones, and water-entry points were identified primarily through manual interpretation of the borehole TV images, based on borehole-wall integrity

and water seepage. The interpretation results were further compared with drilling records, cuttings interpretation, and water inflow monitoring data. During imaging, no slurry was injected, and the drill rods were not rotated. The probe depth was verified using the drill pipe push length. Water-entry points, open fractures, and broken rock-mass intervals were recorded along with their corresponding depths. The device's operating temperature range is −15 °C to 60 °C, and it can operate continuously for up to 9 days. Table 4 outlines the parameters of the borehole TV device.



Figure 7. The object pictures of the coring drilling tool.

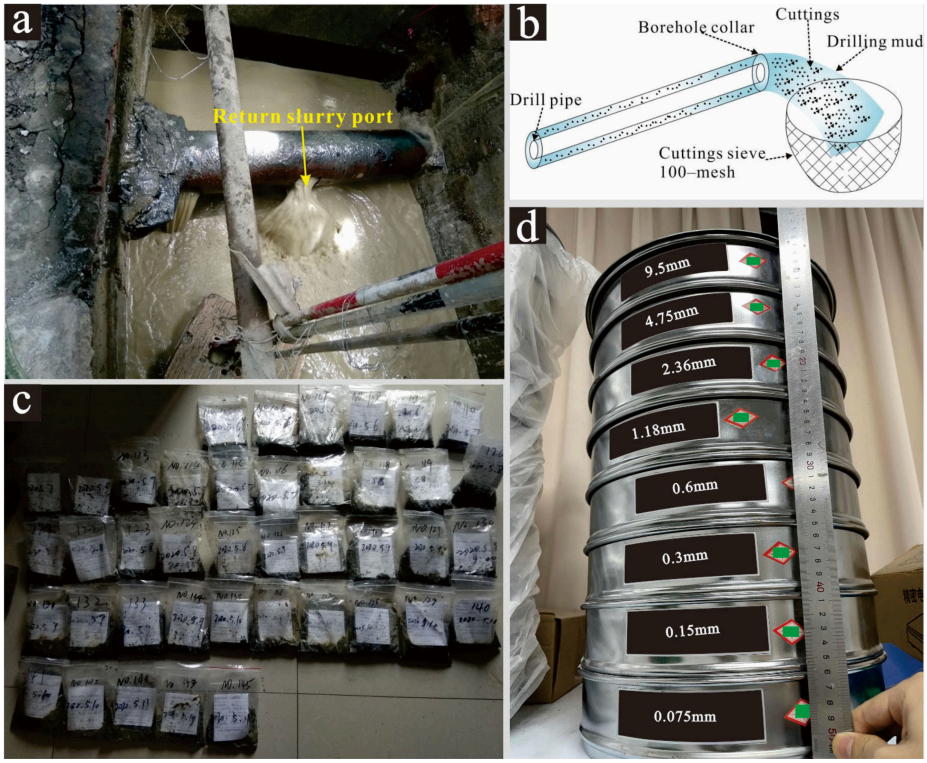


Figure 8. Cutting collection, labeling, and sieving. (**a**) Drilling-fluid returns at the borehole collar; (**b**) a schematic of cutting collection; (**c**) cutting labeling; (**d**) cutting sieving.



Figure 9. Borehole TV system.

Table 4. The technical parameters of the probe.

Item	Technical Parameter
Protection	IP67, Airtight protection
Working temperature	−15~60 °C
Best applicable pipe diameter	250~1200 mm
Material	Stainless steel, aluminum (anti-corrosion treatment)
Lighting source	6 pcs 3 W Flood LED Lights
Imaging system	Color 1/2.5″, Two million pixels (1920 × 1080) CMOS, Angle of view 130°, Sensitivity 0.1 Lux
Camera part	10 mm thick tempered glass
Integrated wiper function	Starting frequency 3 times/min
Lens heating film function	Start up automatically

3.3.3. The Monitoring and Prediction Method of Tunnel Water Inflow

When the HDD rig stops drilling for more than 2 h, the slurry gushing from the hole will become a steady flow of pore water and bedrock-fissure water. As illustrated in Figure 10, a scale was installed at the center of the pool to measure the slurry height, enabling calculation of the water flow rate from the recorded volume and time duration.



Figure 10. The monitoring method of water flow rate in the hole.

Based on the monitored borehole inflow data, tunnel water inflow during construction was predicted using several commonly used analytical and empirical methods, including the Kosgakov formula, the Goodman empirical formula, the Oshima Yoshi formula [24–26], and the empirical formula for railway survey [9]. The formulas and parameter definitions are summarized in Table 5.

Table 5. Formulas for calculating tunnel water inflow.

Method	Formula	Equation No.	Definition of Symbols
Kosgakov formula	$Q_s = \frac{2\alpha K H_0 L}{\ln R - \ln r}$	(1)	Q_s: Predicted steady-state groundwater inflow through the tunnel (m^3/d); K: permeability coefficient of the surrounding rock (m/d); H_0: vertical distance from the original static water level to the center of the equivalent circular tunnel section (m); S: drawdown of groundwater level (m); L: tunnel length within the aquifer (m); R: radius of influence of tunnel inflow (m); r: radius of the equivalent circular tunnel cross-section (m), generally 3.5 m for a single tunnel and 7 m for a twin tunnel.
	$\alpha = \frac{\pi}{2} + \frac{H_0}{R}$	(2)	
Goodman's empirical formula	$Q_s = L\frac{2pKH}{\ln(\frac{4H}{d})}$	(3)	Q_s: Predicted maximum groundwater inflow into the tunnel through the aquifer (m^3/d); L: tunnel length within the aquifer (m); K: permeability coefficient of the surrounding rock (m/d); H: vertical distance from the original static water level to the center of the equivalent circular tunnel section (m); d: diameter of the equivalent circular tunnel section (m), ($d = 2r$).
Oshima Yoshi formula	$Q_s = \frac{2\pi mK(H-r)L}{\ln[4(H-r)/d]}$	(4)	(Q_s): Predicted maximum possible groundwater inflow into the tunnel within the aquifer (m^3/d); K: permeability coefficient of the surrounding rock (m/d); H: vertical distance from the original static water level in the aquifer to the tunnel invert (m); L: tunnel length within the aquifer (m); d: diameter of the equivalent circular tunnel section (m), ($d = 2r$); (m): conversion factor, generally taken as 0.86.
Empirical formula for railway survey	$q_0 = 0.0255 + 1.9224KH$	(5)	q_0: Predicted maximum groundwater inflow through the tunnel (m^3/d); q_s: predicted normal groundwater inflow through the tunnel (m^3/d); K: permeability coefficient of the surrounding rock (m/d); H: vertical distance from the original static water level to the tunnel invert (m).
	$q_s = KH(0.676 - 0.06K)$	(6)	

4. Results

4.1. Three-Dimensional Trajectory Diagram of Boreholes and Tunnel Centerline

Using an HDD guidance system, the inclination, azimuth, and measured depth at each station along the borehole can be acquired in real time. Taking the known geographic coordinates (x_0, y_0, z_0) of the borehole collar as the reference, the three-dimensional coordinates of each survey point along the borehole are computed from the following relations [14]:

$$\begin{aligned} x_{n+1} &= x_n + L\sin\beta_0\cos\psi \\ y_{n+1} &= y_n + L\sin\beta_0\sin\psi \\ z_{n+1} &= z_n + L\cos\beta_0 \end{aligned} \quad (7)$$

where (x_n, y_n, z_n) and $(x_{n+1}, y_{n+1}, z_{n+1})$ denote the spatial coordinates of the n-th and (n + 1)-th measurement points, respectively, and L, β_0, and ψ are the measured depth, inclination, and azimuth at the corresponding survey point within the borehole.

The calculated three-dimensional coordinates of the borehole and the tunnel axis were plotted to obtain a 3D trajectory, as shown in Figure 11, from which the spatial relationship

between the borehole trajectory and the tunnel axis can be analyzed. The tunnel has a vertical excavation height of 8 m and a horizontal excavation width of 12.1 m.

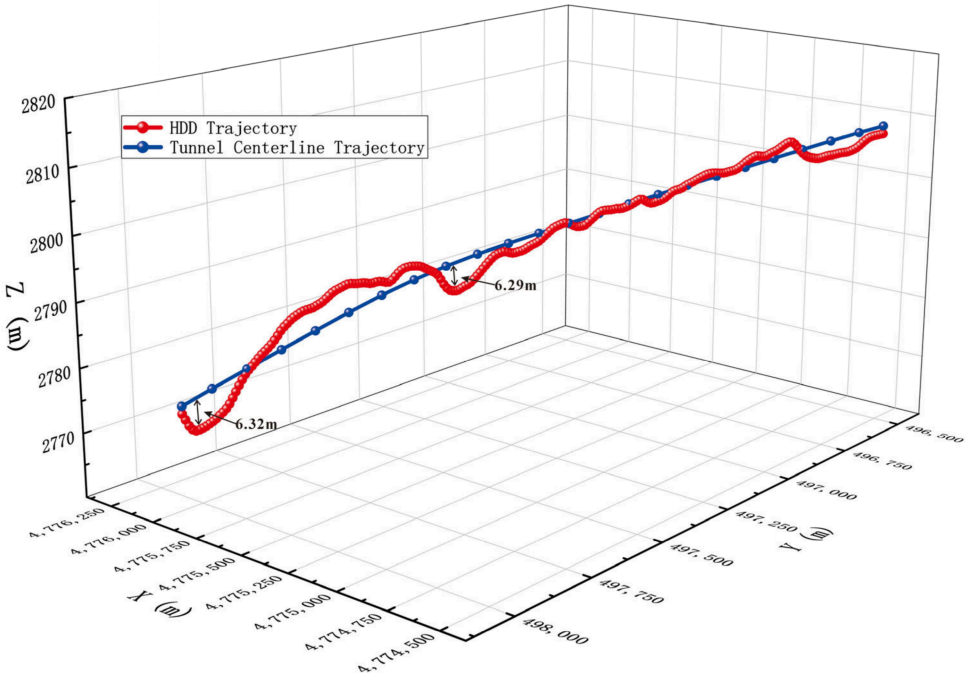


Figure 11. A diagram of HDD trajectory and tunnel design centerline trajectory.

Figure 11 shows the spatial relationship between the 2271 m HDD borehole trajectory and the designed tunnel centerline. The red line represents the HDD borehole trajectory, whereas the blue line represents the tunnel design centerline. The borehole locally deviated outside the tunnel excavation envelope in two intervals. In the interval from 9.17 m to 133 m, the maximum offset from the tunnel centerline was 6.32 m at a measured depth of 56.71 m, exceeding the tunnel excavation envelope by 2.32 m. In the interval from 787.99 m to 883.32 m, the borehole again deviated outside the excavation envelope, with a maximum offset of 6.29 m at a measured depth of 825.56 m, exceeding it by 2.29 m.

4.2. XRD Experimental Analysis Results of Cutting Samples

Based on the preliminary investigation, the lithologies distributed within the tunnel-area HDD investigation zone include tuffaceous sandstone, granodiorite, carbonaceous slate, quartz schist, and gneissic granite. However, the detailed lithological distribution along the tunnel axis still requires further refinement. Therefore, by integrating macroscopic observations of the cuttings with XRD analysis and considering the cuttings' color, texture/structure, and mineralogical composition, the lithological distribution of the borehole surrounding rock can be delineated in greater detail and with improved accuracy.

4.2.1. Calculation of Cutting-Lag Distance

Cuttings require a finite time to travel from the bottom of the borehole to the wellhead. During this transport, the bit continues to advance; therefore, the depth recorded when cuttings are collected at the wellhead does not represent the cuttings' actual borehole position [27]. The exact position should be evaluated as the recorded depth minus the bit advance that occurred over the lag time of the cuttings. The expression is given by:

$$L_{actual} = L_{recorded} - L_{lag} \quad (8)$$

$$L_{lag} = ROP \cdot \frac{L_{recorded}}{v_s} \quad (9)$$

$$v_s = \frac{Q}{\pi(D^2 - d^2)} \quad (10)$$

where L_{actual} (m) is the actual borehole depth, $L_{recorded}$ (m) is the recorded depth at the time of cutting collection, L_{lag} (m) is the cutting-lag distance, ROP (m/h) is the rate of penetration, and v_s (m/s) is the cutting transport velocity; when cuttings are transported in suspension within the borehole, the cutting transport velocity v_s is equal to the annular drilling-fluid velocity [28]. In this study, the annular flow rate is Q = 1800 L/min, the borehole diameter is D = 250 mm, and the drill-rod diameter is d = 168 mm.

As shown in Figure 12a, the overall ROP decreases with increasing drilling depth. The ROP reaches a maximum of 23.85 m/h at a borehole depth of 424 m and decreases to a minimum of 2.5 m/h at 2271 m. As calculated, the maximum cutting-lag distance in Figure 12b is 7.89 m for cutting sample No. 207. The corrected actual borehole depth for each cutting sample is shown in Figure 12c.

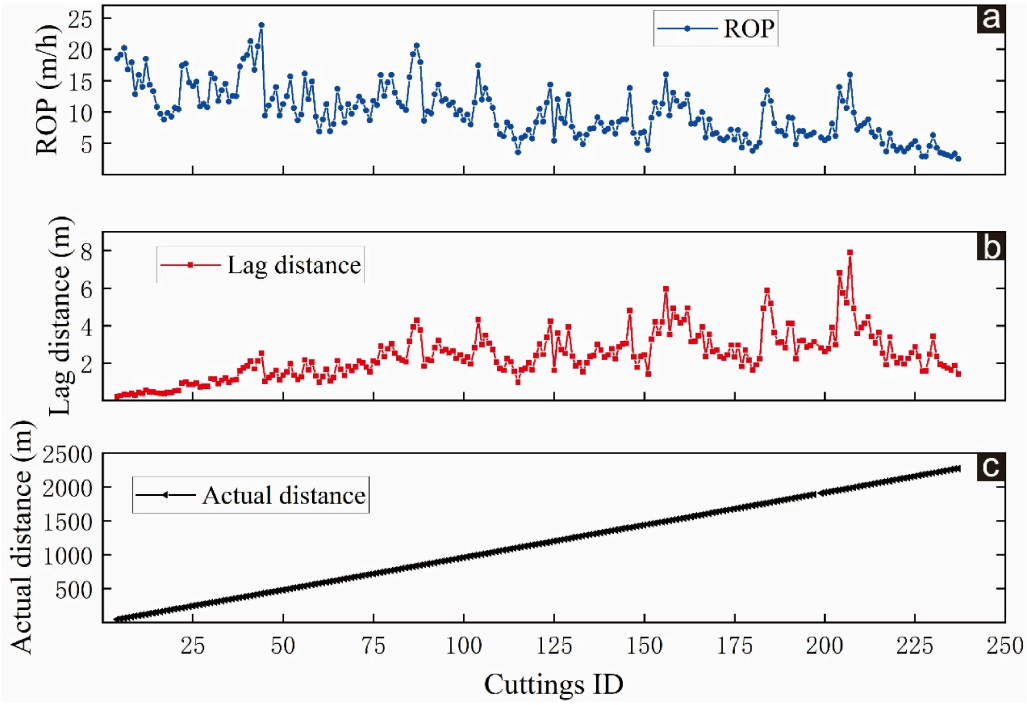


Figure 12. The actual borehole depth corresponding to the cuttings. (**a**) The ROP at the time of cutting collection; (**b**) the lag distance for the cuttings of different IDs; (**c**) the actual borehole depth for the cuttings of different IDs.

4.2.2. Lithological Classification of the Borehole Surrounding Rock

As shown in Figure 13, most of the collected cuttings fall within the particle-size range of 0.3–2.36 mm, while a small proportion exhibit diameters larger than 9.5 mm. XRD analysis has been used in engineering geology to identify the mineral composition of altered and fractured rock materials, including framework minerals and clay minerals such as quartz, feldspar, chlorite, amphibole, and illite [29–33]. The possible influence of drilling-fluid additives on XRD results was also considered. Considering the possible influence of bentonite and polymer residues on clay-mineral signals in XRD patterns, clay-mineral peaks were interpreted cautiously. Lithological classification was based mainly on dominant mineral assemblages identified by XRD, corrected borehole depths of cuttings, previous geological investigation data, and limited core verification, rather than on clay-

mineral content alone. The refined lithological classification of the borehole surrounding rock is summarized in Table 6.

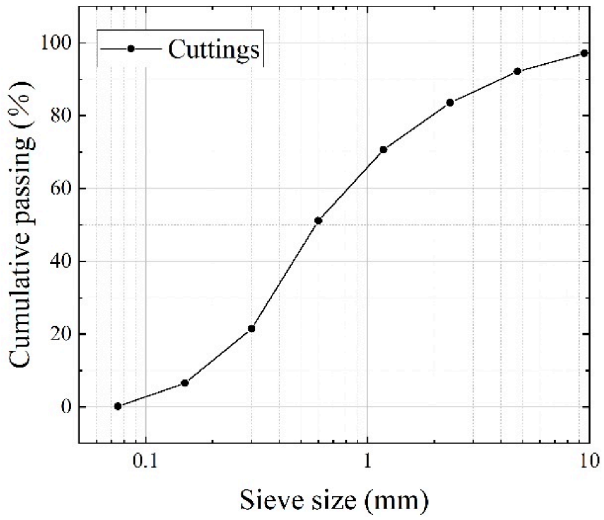


Figure 13. Cutting particle-size distribution.

According to Table 6 and Figure 14, the lag-corrected cuttings, XRD results, macroscopic observations, previous investigation data, and local core verification indicate that the borehole surrounding rock can be divided into five principal lithological units. These units are tuffaceous sandstone from 0.0 to 1605.0 m, granodiorite from 1605.0 to 1748.8 m and from 1769.8 to 1975.6 m, carbonaceous slate from 1748.8 to 1769.8 m, quartz schist from 1975.6 to 2088.3 m, and gneissic granite from 2088.3 to 2271.0 m.

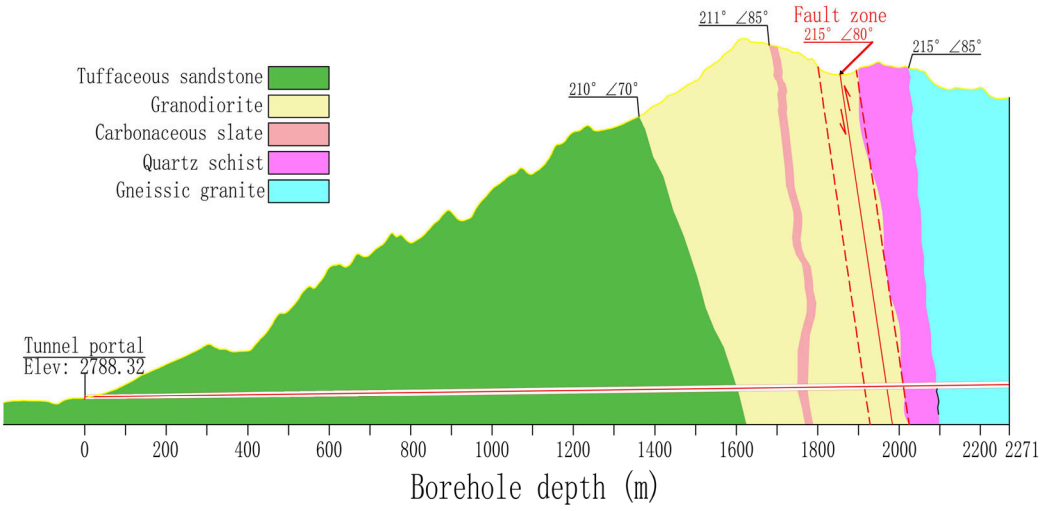


Figure 14. The geological profile of the tunnel in the HDD investigation area. The colored blocks represent different lithologies. The red dashed lines indicate the inferred fault-zone boundaries, the red arrows and red text indicate the fault zone and its attitude, and the black/gray arrows and text indicate the attitude of geological layers.

4.2.3. Coring

One coring was completed at 1900 m of the borehole at the Bolokenu Aqikekuduke fault zone. Figure 15 shows the core obtained from 1900.29 m to 1902.49 m. The core diameter is 101 mm, and its length is 2.2 m. The core has a 95% recovery and an RQD of 48%. The lithology is verified as granodiorite. Some key parameters are summarized in Table 7.



Figure 15. Image of 1900.29 m to 1902.49 m rock cores.

Table 6. Lithological division of the surrounding rock along the borehole.

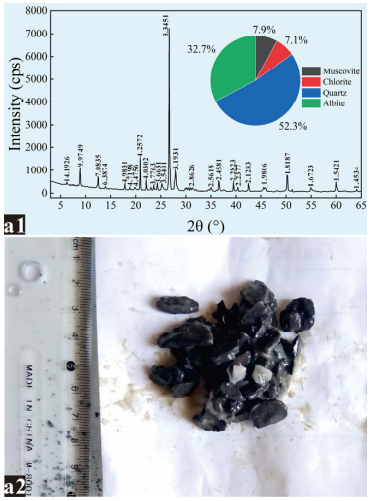
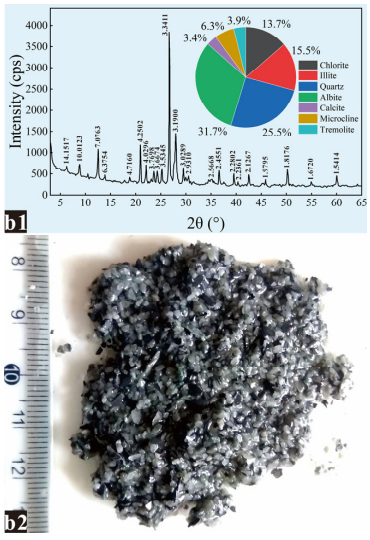
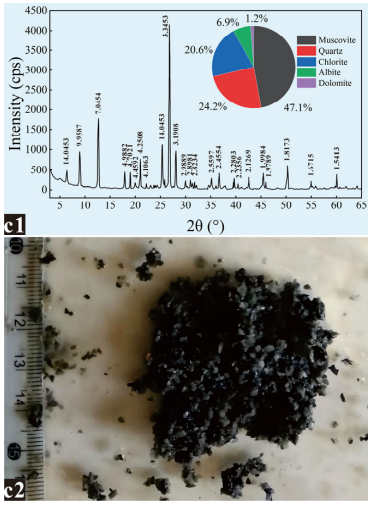
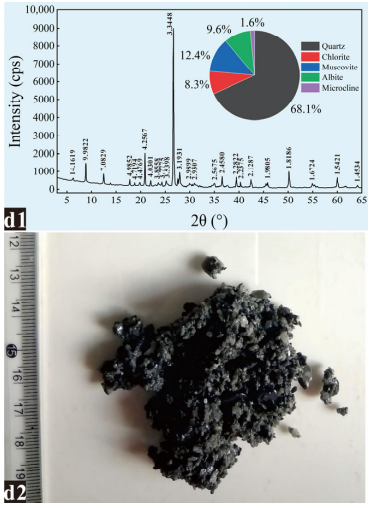
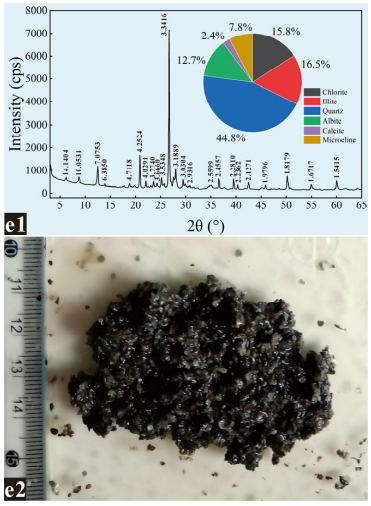
XRD Analysis and Photographs of Cuttings	Characteristics	Lithology
	The cuttings at 361 m are gray-green in color and are dominated by a clastic texture. Quartz and feldspar account for approximately 85%, while the occurrence of mica and chlorite is likely related to a tuffaceous matrix and/or volcanic alteration. Overall, these features are consistent with tuffaceous sandstone.	Tuffaceous sandstone (0.0~1605.0 m)
	The cuttings at 1747.5 m are gray-white and dominated by feldspar and quartz, indicating a granitic/dioritic framework. Elevated illite and chlorite contents suggest alteration such as sericitization and chloritization. Minor calcite likely represents fracture infilling. Overall, these features are consistent with granodiorite.	Granodiorite (1605.0~1748.8 m; 1769.8~1975.6 m)

Table 6. *Cont.*

XRD Analysis and Photographs of Cuttings	Characteristics	Lithology
	The cuttings at 1757 m are dark gray. Mica and chlorite account for approximately 68%, indicating a well-developed slaty structure controlled by platy minerals. The dark color suggests the presence of carbonaceous material, although XRD may not clearly detect it. Overall, these features are consistent with carbonaceous slate.	Carbonaceous slate (1748.8~1769.8 m)
	The cuttings in 1986 m are dark gray in color. Quartz accounts for 68.3%, while mica and chlorite contribute to the schistosity; feldspar is minor. Overall, these features are more consistent with quartz schist.	Quartz schist (1975.6~2088.3 m)
	The cuttings at 2197.8 m are gray-brown. Quartz, together with two feldspar phases (albite and microcline), indicates a granitic composition. Elevated illite and chlorite contents suggest gneissification and shear-related alteration, which is consistent with gneissic granite.	Gneissic granite (2088.3~2271.0 m)

Note: (a1) XRD pattern and mineral composition of the cuttings collected at 361.0 m; (a2) corresponding photograph of the cuttings collected at 361.0 m; (b1) XRD pattern and mineral composition of the cuttings collected at 1747.5 m; (b2) corresponding photograph of the cuttings collected at 1747.5 m; (c1) XRD pattern and mineral composition of the cuttings collected at 1757.0 m; (c2) corresponding photograph of the cuttings collected at 1757.0 m; (d1) XRD pattern and mineral composition of the cuttings collected at 1986.0 m; (d2) corresponding photograph of the cuttings collected at 1986.0 m; (e1) XRD pattern and mineral composition of the cuttings collected at 2197.8 m; (e2) corresponding photograph of the cuttings collected at 2197.8 m.

Table 7. Parameter table of granodiorite from 1900.29 m to 1902.49 m.

Items	Core Parameters
Natural density	2.85 g/cm^3
Water absorption	0.39%
Coefficient of water saturation	0.70%
Saturation coefficient	0.56
Uniaxial compressive strength	77.2 MPa
Elastic modulus	104.2 GPa
Elastic Poisson's ratio	0.28

4.3. Tunnel Water Inflow Calculation

4.3.1. Borehole Water Inflow Monitoring and Permeability Coefficient Estimation

Based on the time-dependent inflow rate monitored in the HDD investigation borehole, the tunnel water inflow during construction can be estimated. Figure 16 shows the variation in the borehole inflow rate with borehole depth along the 2271 m drilling section.

As shown in Figure 16, the borehole inflow rate generally increases with increasing drilling depth. When the cumulative drilling depth reached 418 m, the total borehole inflow rate increased to 18 m^3/h. Thereafter, although the total inflow rate fluctuated with further drilling, it reached a maximum value of 45.57 m^3/h at a borehole depth of 2271 m. Table 8 lists the incremental increases in borehole inflow rate for different borehole intervals and presents the calculated permeability coefficient of the surrounding rock and the tunnel inflow radius of influence. It should be noted that the hydraulic head H in Table 8 does not represent the tunnel overburden thickness. Instead, H is the effective hydraulic head used for seepage calculation. In this study, H was obtained from hydraulic-head measurements in vertical boreholes and was assigned to the corresponding HDD borehole intervals. Therefore, the H values in Table 8 represent interval-specific groundwater heads, not rock-cover thicknesses. This explains why they are lower than the maximum tunnel overburden, which is approximately 1200 m.

Table 8. Parameters for tunnel water inflow calculation.

Depth (m)	Incremental Groundwater Inflow Q (m^3/h)	Hydraulic Head H (m)	Borehole Diameter d_0 (m)	Hydraulic Conductivity K (m/d)	Tunnel Radius of Influence R (m)
0–293	11.00	17.5	0.25	0.0514	241.7
293–530	9.00	50	0.25	0.0368	234.3
530–634	2.00	150	0.25	0.0035	218.3
634–1003	4.29	300	0.25	0.00125	216.1
1003–1900	17.19	400	0.25	0.0016	216.3
1900–2102	13.41	400	0.25	0.0088	220
2102–2271	14.80	638	0.25	0.00484	218

The permeability coefficient of the surrounding rock was calculated using the Goodman empirical formula [34]:

$$\mathrm{K} = \frac{Q \ln \frac{4H}{d_0}}{2\pi LH} \tag{11}$$

where Q_0 (m^3/d) is the measured water inflow of the tunnel (or borehole) per unit length; H (m) is the aquifer thickness or the burial depth (i.e., the range of influence of groundwater head); d_0 (m) is the diameter of the tunnel or borehole; and L (m) is the length of the considered interval.

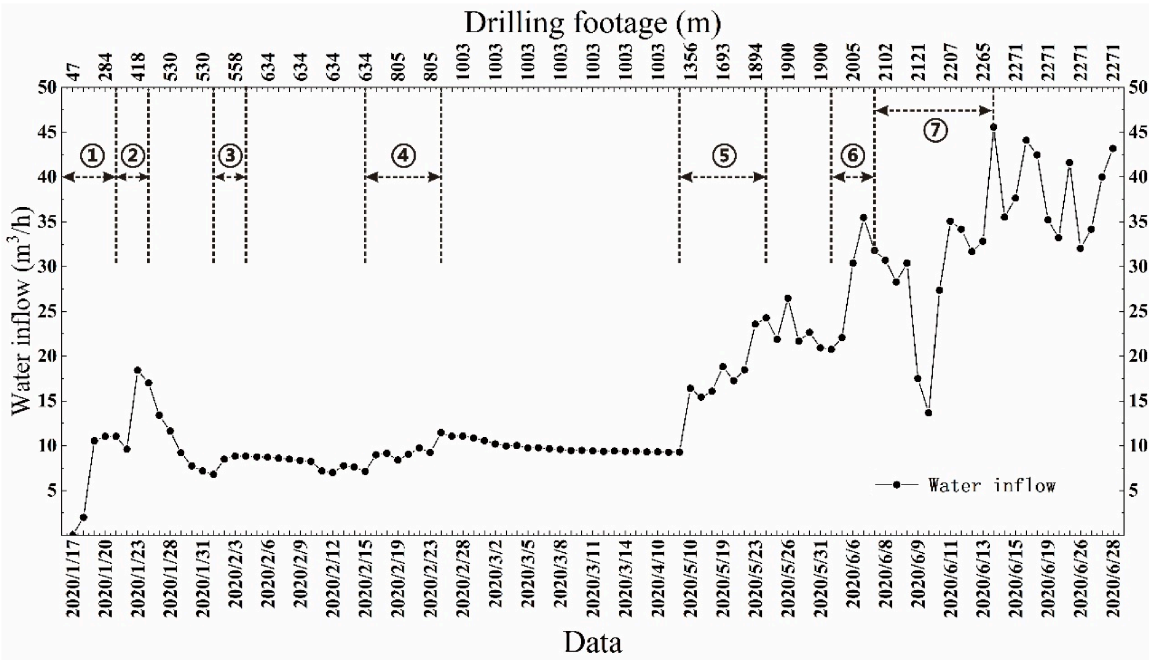


Figure 16. Variation in water inflow with drilling footage and observation date. The circled numbers (1)–(7) indicate seven borehole-depth intervals: (1) 0–293 m, (2) 293–530 m, (3) 530–634 m, (4) 634–1003 m, (5) 1003–1900 m, (6) 1900–2102 m, and (7) 2102–2271 m.

The radius of influence R is given by:

$$R = 215.5 + 510.5K \tag{12}$$

For fault zones, the radius of influence R is:

$$R = 2H\sqrt{HK} \tag{13}$$

4.3.2. Prediction of Tunnel Water Inflow During Construction

Since groundwater in the mountain massif is predominantly hosted in an unconfined aquifer, tunnel water inflow during construction was predicted using the methods described in Section 3.3.3 and the parameters listed in Table 9. The prediction results are summarized in Table 9.

Table 9. Results of tunnel water inflow calculation.

Depth Interval (m)	Goodman (q_s) (m^3/(d·m))	Kosgakov (q_s) (m^3/(d·m))	Empirical Formula for Railway Survey (q_s) (m^3/(d·m))	Oshima Yoshi (q_s) (m^3/(d·m))	Goodman (Q_s) (m^3/d)	Kosgakov (Q_s) (m^3/d)	Empirical Formula for Railway Survey (Q_s) (m^3/d)	Oshima Yoshi (Q_s) (m^3/d)
0–293	2.670	0.444	0.605	2.004	782.3	130.2	177.3	587.2
293–530	3.651	0.916	1.240	2.957	865.3	217.1	293.8	700.9
530–634	0.773	0.266	0.355	0.651	80.4	27.7	36.9	67.7
634–1003	0.475	0.190	0.253	0.404	175.4	70.3	93.5	149.1
1003–1900	0.767	0.325	0.433	0.654	687.6	291.6	388.0	586.3
1900–2102	4.216	1.780	2.378	3.595	851.6	359.6	480.3	726.1
2102–2271	3.396	1.565	2.087	2.905	574.0	264.5	352.6	490.9

As shown in Table 9, the predicted normal inflow values differ among the four methods. The Goodman empirical formula gives a total normal inflow of 4016.6 m^3/d, compared

with 1361.0 m^3/d from the Kosgakov formula, 1822.4 m^3/d from the railway empirical formula, and 3308.2 m^3/d from the Oshima Yoshi formula. The Goodman result is approximately 2.95 times the Kosgakov result and 2.20 times the railway empirical result, but only slightly higher than the Oshima Yoshi result. After applying a conservative amplification factor of 3.0 to the Goodman normal inflow, the maximum tunnel inflow was estimated as 12,049.8 m^3/d.

4.3.3. Borehole Tv-Based Localization of Inflow Points and Fracture Zones

The tunnel water inflow has been predicted above based on observations from the borehole inflow. In addition, borehole TV can be used to precisely identify borehole water-entry points and intervals with well-developed joints and fractures. Figure 17 shows locations where borehole inflow is relatively pronounced, whereas Figure 18 presents intervals where joints and fractures are more intensively developed.

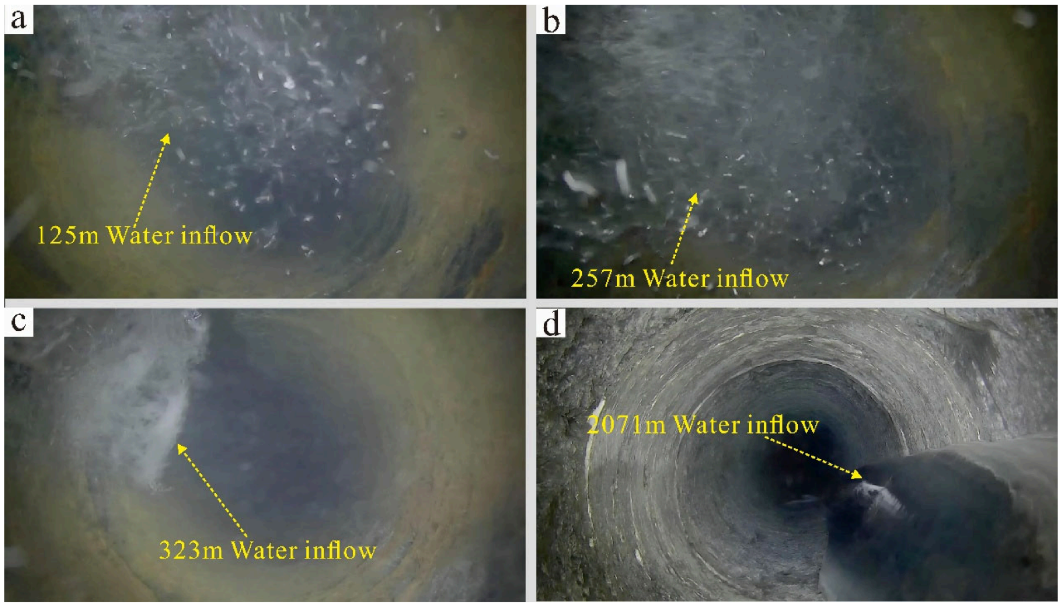


Figure 17. Borehole intervals exhibiting groundwater inflow from the surrounding rock. (**a**) Water-entry point at a borehole depth of 125 m; (**b**) water-entry point at a borehole depth of 257 m; (**c**) water-entry point at a borehole depth of 323 m; (**d**) water-entry point at a borehole depth of 2071 m.

As indicated in Figure 17, pronounced groundwater discharge from bedrock fractures occurs at borehole depths of 125 m, 257 m, 323 m, and 2071 m. In conjunction with Figure 16, it can be observed that once the drilling depth exceeds 323 m, the borehole inflow increases sharply, with a marked surge at a depth of 418 m.

As shown in Figure 18, joints and fractures are relatively well-developed at borehole depths of 555 m, 1038 m, 1046 m, and 1947 m. Based on visual interpretation of the borehole TV images, approximately two major visible fractures are identified at 555 m, five major fractures at 1038 m, about seven major fractures at 1046 m, and about six major fractures at 1947 m. In particular, the intervals at 1046 m and 1947 m exhibit more intensive fracture development, with several open or semi-open fractures and local borehole wall spalling. Some small dark spots and irregular pits on the borehole wall were interpreted as possible microfractures, spalling pits, or mud adhesion features, and were therefore not included in the main fracture count. These observations indicate that the surrounding rock at these depths is fractured to locally broken. Accordingly, enhanced protective and reinforcement measures should be implemented when tunnel excavation reaches these sections.

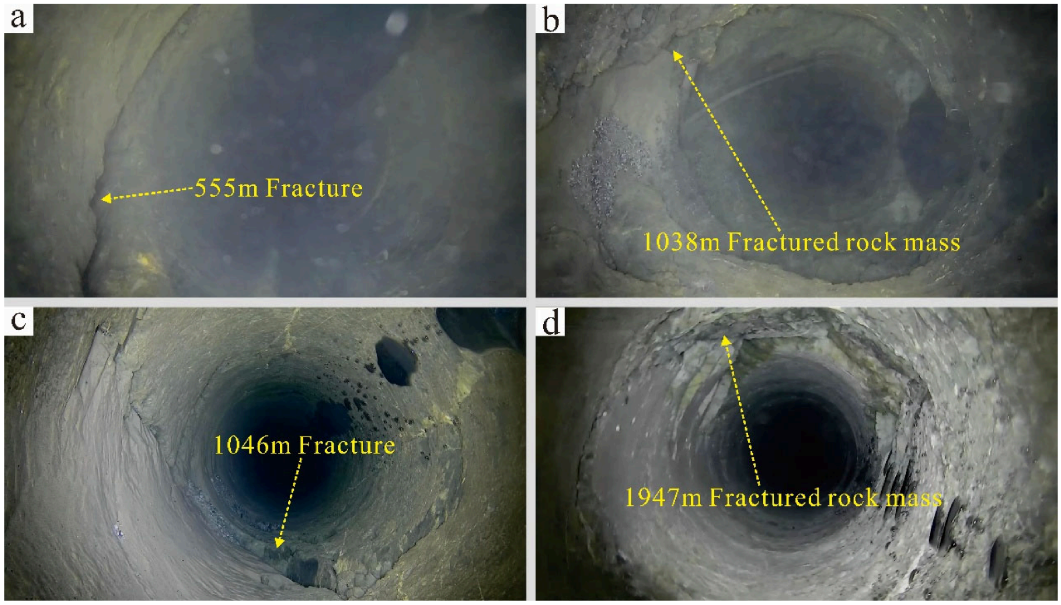


Figure 18. Development of joints and fractures in the borehole surrounding rock. (**a**) Fractures in the surrounding rock at a borehole depth of 555 m; (**b**) highly fractured surrounding rock at a borehole depth of 1038 m; (**c**) fractures in the surrounding rock at a borehole depth of 1046 m; (**d**) well-developed fractures and severely fractured rock mass in the Boa Fault Zone segment.

5. Discussion

5.1. Trajectory-Control Performance and Spatial Representativeness

As shown in Figure 11, the red HDD trajectory and the blue tunnel design centerline are generally close to each other over the 2271 m investigation length, indicating that the borehole can provide representative along-axis geological information for most of the investigated section. However, Figure 11 also clearly shows two local deviation intervals, namely 9.17–133 m and 787.99–883.32 m. The maximum offsets in these two intervals are 6.32 m and 6.29 m, respectively, exceeding the tunnel excavation envelope by 2.32 m and 2.29 m. Therefore, the figure demonstrates both the overall representativeness of the HDD borehole and the local intervals where geological interpretation should be treated with caution.

The spatial pattern in Figure 11 further indicates that trajectory-control accuracy and geological investigation accuracy should be evaluated separately. Although the borehole trajectory is generally consistent with the tunnel alignment, the locally deviated intervals may introduce uncertainty in the direct spatial representativeness of cuttings, borehole TV observations, and water-entry interpretations, particularly for small-scale fractures, local weak zones, and highly heterogeneous rock masses. In this project, the offsets were mainly attributed to magnetic or geomagnetic interference from metallic materials in the tunnel environment, including tunnel-lining reinforcement, steel supports, rock bolts, wire mesh, pipelines, and construction equipment [35]. Therefore, geological information from the locally deviated intervals should be interpreted as evidence from the adjacent rock mass near the tunnel axis rather than as exact observations within the excavation envelope.

5.2. Reliability of Cutting-Lag Correction and Lithological Interpretation

The cutting-lag correction is essential for HDD-based tunnel investigation because the collected cuttings do not correspond directly to the bit position at the time of sampling [36,37]. Figure 12a shows that the ROP generally decreases with increasing drilling depth, which directly affects the lag distance of transported cuttings. Figure 12b indicates that the maximum lag distance is 7.89 m, and Figure 12c further shows the corrected

actual borehole depth corresponding to each cutting sample. Although this lag distance is small relative to the total borehole length, it is important for identifying local lithologic transitions. Therefore, the corrected depths improve the spatial consistency among cuttings, XRD results, local core verification, and the reconstructed geological profile.

The figure-based lithological interpretation also supports the reliability of the HDD-derived geological profile. Figure 13 shows that most cuttings fall within the particle-size range suitable for macroscopic observation and XRD-based mineralogical identification, whereas Figure 14 integrates the corrected cutting depths, XRD results, macroscopic observations, and preliminary investigation information into a continuous geological profile along the HDD borehole. In addition, Figure 15 and Table 7 provide local core verification for the granodiorite interval at 1900.29–1902.49 m. Compared with previous surface geological mapping and preliminary investigation results, HDD provides more continuous geological information directly along the tunnel axis. However, small-scale lithological boundaries remain constrained by the 10 m sampling interval, the limited number of cores, and the possible mixing of cuttings during long-distance mud circulation.

5.3. Hydrogeological Interpretation and Selection of the Water-Inflow Prediction Method

The borehole inflow monitoring results show a general increase in inflow with drilling depth. As shown in Figure 16, the borehole inflow does not increase uniformly. Still, it exhibits stage-like changes and local abrupt increases, suggesting that groundwater occurrence in the investigated section is mainly controlled by fracture development, fault-related damage zones, and lithologic contacts rather than by homogeneous porous seepage. This interpretation is supported by Figure 17, which directly identifies water-entry points, and by Figure 18, which shows fracture-rich intervals in the borehole wall images.

The predicted tunnel water inflow varies among the four calculation methods because each method is based on different physical assumptions and hydrogeological simplifications. Table 8 summarizes the hydraulic parameters used in the calculations, and Table 9 shows that the Goodman empirical formula yields the highest normal inflow estimate of 4016.6 m^3/d and a conservative maximum inflow estimate of 12,049.8 m^3/d after applying the amplification factor. Therefore, the Goodman result was selected as the recommended estimate because it better reflects construction-stage risk under fractured, high-head mountain-tunnel conditions. However, the method assumes a circular tunnel, steady seepage, and a homogeneous and isotropic aquifer, and Muskat–Goodman-type approximations may deviate from exact analytical solutions even under idealized conditions [38]. Therefore, the Goodman result should be interpreted together with HDD borehole inflow monitoring and borehole TV observations. Considering the possible increase in permeability induced by excavation in fractured rock masses, a conservative amplification factor of 3.0 was applied following Gattinoni and Scesi [39].

The comparative results in Table 9 also help clarify the applicability of different prediction methods. The Kosgakov formula is more suitable for relatively stable inflow in phreatic aquifers within a defined radius of influence and under drawdown conditions. In contrast, the Goodman formula is commonly applied to trans-ridge or adjacent mountain tunnels crossing water-bearing zones and provides a more conservative estimate under high-head drainage conditions [40]. Because the visual evidence in Figures 17 and 18 indicate fracture-controlled groundwater pathways, and the hydraulic conductivity was back-calculated from monitored inflow data from the HDD boreholes; the Goodman result was adopted as the recommended construction-stage inflow estimate. At the same time, the other methods were retained as comparative references.

5.4. Engineering Implications of Borehole TV Observations

The borehole TV results provide direct visual evidence for water-entry points and fracture-rich intervals that cannot be fully resolved by cuttings or inflow monitoring alone. In Figure 17, the water-entry points at 125 m, 257 m, 323 m, and 2071 m show localized seepage or inflow from the borehole wall, indicating preferential groundwater channels formed by bedrock fractures or local broken zones. In Figure 18, the fracture-rich intervals at 555 m, 1038 m, 1046 m, and 1947 m exhibit pronounced discontinuities and locally broken borehole walls, indicating reduced rock-mass integrity. When interpreted together with the inflow trend in Figure 16, these borehole TV images indicate that the main hydrogeological risk is controlled by discrete fracture zones rather than by uniform seepage along the whole borehole. These intervals should therefore be treated as key zones for advanced water control, support design, and construction risk management.

6. Conclusions

This study applied HDD to the geological investigation of the portal section of the Tianshan Shengli Tunnel. A 2271 m long directional investigation borehole was completed along the tunnel axis, and cutting analysis, targeted coring, borehole inflow monitoring, and borehole TV imaging were integrated to characterize lithology, water inflow, and fracture development. The main conclusions are as follows:

1. The field test demonstrates that HDD can provide continuous geological information along the tunnel alignment. The maximum offset between the HDD borehole and the tunnel axis was 6.32 m, and most of the borehole remained within or close to the tunnel excavation section. This confirms the feasibility of using HDD for refined geological investigation of super-long tunnels.

2. The cutting-lag-distance correction improved the depth accuracy of lithological interpretation. By combining corrected cutting depths, XRD analysis, macroscopic observations, and core verification, the surrounding rock along the borehole was divided into five lithological units: tuffaceous sandstone, granodiorite, carbonaceous killas, quartz schist, and gneissic granite.

3. Borehole inflow monitoring provided useful parameters for predicting tunnel water inflow during construction. The predicted normal inflow of the 2271 m investigation section was 4016.6 m^3/d, and the maximum inflow was estimated as 12,049.8 m^3/d. These results provide a basis for groundwater control during tunnel excavation.

4. Borehole TV imaging enabled direct identification of water-entry points and fractured intervals. Pronounced water inflow was observed at depths of 125 m, 257 m, 323 m, and 2071 m, while well-developed fractures were identified at depths of 555 m, 1038 m, 1046 m, and 1947 m. These intervals should receive special attention during tunnel excavation and support design.

5. This study is based on a single HDD borehole, and the amount of core verification remains limited. In addition, comprehensive logging and hydraulic fracturing tests were not successfully completed because the available downhole tools were not fully compatible with the HDD system. Future work should focus on developing HDD-compatible downhole testing tools to obtain more complete information on rock-mass integrity, hydrogeological conditions, and in situ stress.

7. Limitations and Outlook

Two planned downhole tests were not completed in this study. First, comprehensive borehole logging failed because the available oilfield logging tool string was too long and not fully compatible with the long-distance, inclined-to-horizontal HDD borehole; it was accidentally dropped during deployment. As a result, continuous geophysical logging

data were not obtained. Second, the hydraulic fracturing test failed because the injection pressure could not be built up to the target level, mainly due to insufficient packer sealing and possible leakage along fractures or the borehole wall. Therefore, no reliable in situ stress data were obtained.

These failures reduced the completeness of the investigation. Lithological characterization mainly relied on lag-corrected cuttings, XRD analysis, macroscopic observations, and one local core sample. This dataset can support the identification of major lithological units along the borehole, but small-scale lithological boundaries, fracture-rich zones, and local weak intervals remain less constrained. Therefore, this study should be regarded as an HDD-based geological investigation case with partial downhole testing, rather than a fully verified integrated investigation method. Future work should focus on developing shorter, modular logging tools, HDD-compatible hydraulic fracturing systems, and an oriented, scale-calibrated borehole imaging system for long-distance HDD investigation holes. The logging tools should be improved in terms of tool-string length, modular deployment, and compatibility with inclined-to-horizontal boreholes. The hydraulic fracturing system should be optimized with enhanced packer sealing, anchoring, pressure-holding capacity, and leakage diagnosis [41]. In addition, the borehole imaging system should enable quantitative extraction of fracture orientation, aperture, infilling characteristics, and fracture-frequency parameters from borehole-wall images, thereby improving the reliability of fracture characterization in future HDD-based geological investigations [42].

Author Contributions: Q.Z.: Conceptualization, methodology, data curation, writing—original draft preparation, and investigation. X.Y.: Methodology, data curation, and writing—reviewing. J.L.: Investigation, field coordination, resources, and validation. S.H.: Methodology, writing—reviewing and editing, and validation. B.M.: Conceptualization, methodology, supervision, and validation. All authors have read and agreed to the published version of the manuscript.

Funding: This research was funded by the Hubei Provincial Science and Technology Plan Project, "Key Technologies for Targeted Exploration and Efficient Utilization of Geothermal Energy in Hot Dry Rock near Tunnels" (Grant No. 2025BCB119).

Data Availability Statement: Data will be made available on request.

Conflicts of Interest: Author Qiang Zhao and Jiguo Liu were employed by the company CCCC Second Highway Consultants Co., Ltd., Wuhan. The remaining authors declare that the research was conducted in the absence of any commercial or financial relationships that could be construed as a potential conflict of interest.

References

1. Ma, B.S. *The Science of Trenchless Engineering*; China Communications Press: Beijing, China, 2008. (In Chinese)
2. Yan, X.F.; Ma, B.S.; Zeng, C.; Liu, Y. Analysis of Formation Fracturing for the Maxi-HDD Qin River Crossing Project in China. *Tunn. Undergr. Space Technol.* **2016**, *53*, 1–12. [CrossRef]
3. Anonymous. An example of horizontal drilling in seikan tunnel. *Tunn. Constr.* **1983**, *3*, 98–99. (In Chinese)
4. Zhang, H.; Liu, G.; Wu, J.; Wang, Q.; Yu, H.; Liu, Z.; Xu, J. Technical Scheme for 3000 m Horizontal Directional Drilling for the Sichuan–Tibet Railway. *Explor. Eng.* **2020**, *47*, 1–6. (In Chinese)
5. Chen, X.S.; Xu, Z.H.; Bao, X.H.; Wang, X.T.; Fu, Y.B. Challenges and Technological Breakthroughs in Tunnel Construction in China. *China J. Highw. Transp.* **2020**, *33*, 1–14.
6. Yan, J.X. Technical Challenges of Super-Long Mountainous Tunnels at Great Depth. *Mod. Tunn. Technol.* **2018**, *55*, 1–5. [CrossRef]
7. Shu, B.; Ma, B.S.; Sun, P.H. *HDD in Rocks*; Central South University Press: Changsha, China, 2021. (In Chinese)
8. Wang, H.M.; Li, J.; Li, Y.; Zhuang, S.; Zhao, Y.; Qian, F. Construction Practice of a Large-Displacement Scientific Borehole with an Ultra-High Water-to-Vertical Ratio in the Main Navigation Channel of Shiziyang. *Drill. Eng.* **2022**, *49*, 135–141. (In Chinese) [CrossRef]
9. Liu, X.L. Predicting tunnel groundwater inflow by geological investigation using horizontal directional drilling technology. *Adv. Civ. Eng.* **2022**, *2022*, 6578331. [CrossRef]

10. Hu, Y.; Yang, Y. A Comparative Study on Drag Reduction Methods for Continental Shale Drilling in the Fuxing Block, Southeastern Sichuan Basin. *Reserv. Sci.* **2026**, *2*, 81–96. [CrossRef]
11. Gao, D.; Diao, B.; Wu, Z.; Zhu, Y. Research into magnetic guidance technology for directional drilling in SAGD horizontal wells. *Pet. Sci.* **2013**, *10*, 500–506. [CrossRef]
12. Tang, F.; Yang, J.; Li, H.-N.; Liu, F.; Wang, N.; Jia, P.; Chen, Y. Field Validation of a Magnetic Sensor to Monitor Borehole Deviation during Tunnel Excavation. *Materials* **2018**, *11*, 1511. [CrossRef] [PubMed]
13. Yu, F.; Huang, G.; Ni, H.; Nie, Z.; Li, W.; Li, J.; Jiang, W. Analysis of the Main Factors Affecting Bottom Hole Assembly Re-Entry into Main Hole in Forward Drilling of Fishbone Wells. *J. Pet. Sci. Eng.* **2020**, *189*, 107018. [CrossRef]
14. Xu, T.; Jiang, B.; Chen, X.L.; Shi, Y. Design of an underground attitude measuring sonde for directional drilling locator. In Proceedings of the 2016 3rd International Conference on Information Science and Control Engineering, Beijing, China, 8–10 July 2016; pp. 929–932. [CrossRef]
15. Sun, Y.; Shao, K.; Wang, Z.; Fan, Y.; Chen, D. An Intelligent Directional Drill Steering Method Based on Real-Time Adaptive Closed-Loop Control. *Processes* **2025**, *13*, 3798. [CrossRef]
16. Liu, X.; Jiang, Z.; Wang, Y.; Mo, H.; Li, H.; Guo, J. Research on Trajectory Control Technology for L-Shaped Horizontal Exploration Wells in Coalbed Methane. *Sci. Rep.* **2024**, *14*, 11343. [CrossRef] [PubMed]
17. Zhang, N.; Li, F.; Ren, B.; Liu, Z.; Wang, D.; Chen, J.; Lyu, F. Research on Wellbore Trajectory Control of Rotary Steerable System Using Back-Propagation Neural Network-Fuzzy Method. *Geoenergy Sci. Eng.* **2025**, *257*, 214201. [CrossRef]
18. Royal, A.C.D.; Riggall, T.J.; Chapman, D.N. Analysis of steering in horizontal directional drilling installations using down-hole motors. *Tunn. Undergr. Space Technol.* **2010**, *25*, 754–765. [CrossRef]
19. Rodríguez, R.; Fernández, V.; Bascompta, M.; Garcia-Gonzalez, H. Directional Core Drilling as an Approach to Reduce Uncertainty in Tunneling Construction. *Appl. Sci.* **2023**, *13*, 10998. [CrossRef]
20. Rostami, J.; Sepehrmanesh, M.; Gharahbagh, E.A.; Mojtabai, N. Planning Level Tunnel Cost Estimation Based on Statistical Analysis of Historical Data. *Tunn. Undergr. Space Technol.* **2013**, *33*, 22–33. [CrossRef]
21. Gisbert, J.; Vallejos, A.; González, A.; Pulido-Bosch, A. Environmental and Hydrogeological Problems in Karstic Terrains Crossed by Tunnels: A Case Study. *Environ. Geol.* **2009**, *58*, 347–357. [CrossRef]
22. Huang, P.; Chen, Z.; Ge, H.; Liu, Z. Seismic Protection of Civil Engineering Constructions with a Side Barrier for Rayleigh Waves: Application to Underground Structures. *Tunn. Undergr. Space Technol.* **2024**, *151*, 105844. [CrossRef]
23. Du, Y.; Wu, C.; Wang, C.; Yuan, G.; Ouyang, S.; Liao, J.; An, Y. Stress background and rock fractures revealed by ultrasonic borehole television in the Fankou Lead-Zinc Mine. *Front. Earth Sci.* **2023**, *11*, 1286335. [CrossRef]
24. Frenelus, W.; Peng, H.; Zhang, J. Evaluation Methods for Groundwater Inflows into Rock Tunnels: A State-of-the-Art Review. *Int. J. Hydrol.* **2021**, *5*, 152–168. [CrossRef]
25. Luo, G.; Bai, W.Z.; Zhang, Y. Comparative analysis of tunnel inflow forecast. In Proceedings of the International Conference on Energy, Power, Environment and Computer Application (ICEPECA), Wuhan, China, 20–21 January 2019.
26. Chen, Y.N.; Liu, M.Y.; Su, M.Z.; Ding, M.X.; Li, H.L.; Jing, Y. Prediction of water inflow and analysis of surrounding rock stability in unfavorable geological mountain tunnel. *Front. Earth Sci.* **2024**, *12*, 1373627. [CrossRef]
27. Wang, C.; Li, S.; Qi, Y.; Zhang, Z.; Zheng, D.; Zhong, H.; Wang, C. Study on the Migration Mechanism of Heterogeneous Cuttings in Long-Reach Horizontal Wells. *Sci. Rep.* **2025**, *15*, 20514. [CrossRef] [PubMed]
28. Ma, L.K. *Study on Cuttings Transport during Drilling in Inclined Section of Complex Structure Wells*; Central South University: Changsha, China, 2022. (In Chinese)
29. Zhao, H.R.; Jiang, Q.; Xia, Y.; Hou, D.Q.; Xu, D.P. Nano-SiO_2 modified microbial-induced carbonate precipitation: Application in altered rock fracture zone reinforcement and strengthening mechanism. *Eng. Geol.* **2026**, *362*, 108531. [CrossRef]
30. Ahmad, S.; Wadood, B.; Khan, S.; Ahmed, S.; Ali, F.; Saboor, A. Integrating the palynostratigraphy, petrography, X-ray diffraction and scanning electron microscopy data for evaluating hydrocarbon reservoir potential of Jurassic rocks in the Kala Chitta Range, Northwest Pakistan. *J. Pet. Explor. Prod. Technol.* **2020**, *10*, 3111–3123. [CrossRef]
31. Reed, M.M.; Ferrier, K.L.; Nachlas, W.O.; Schneider, B.; Arson, C.; Xu, T.; Shen, X.; West, N. A free, open-source method for automated mapping of quantitative mineralogy from energy-dispersive X-ray spectroscopy scans of rock thin sections. *Geosci. Instrum. Methods Data Syst.* **2025**, *14*, 193–209. [CrossRef]
32. Ruiz Cruz, M.D.; Sanz de Galdeano, C.; Lázaro, C. Metamorphic evolution of Triassic rocks from the transition zone between the Maláguide and Alpujárride complexes (Betic Cordilleras, Spain). *Eur. J. Mineral.* **2005**, *17*, 81–91. [CrossRef]
33. Li, Y.K.; Cao, J.J.; Wu, Z.Q.; Dai, D.-L.; Lin, Z.-X. NIR and XRD Analysis of Drill-Hole Samples from Zhamuaobao Iron-Graphite Deposit, Inner Mongolia. *Spectrosc. Spectr. Anal.* **2015**, *35*, 83–88. [CrossRef]
34. Fu, H.; An, P.; Chen, L.; Cheng, G.; Li, J.; Yu, X. Analysis of Tunnel Water Inrush Considering the Influence of Surrounding Rock Permeability Coefficient by Excavation Disturbance and Ground Stress. *Appl. Sci.* **2021**, *11*, 3645. [CrossRef]
35. Yang, C.; Zeng, Q.; Xiong, Z.; Yang, J. IMU/Magnetometer-Based Azimuth Estimation with Norm Constraint Filtering. *Sensors* **2024**, *24*, 2982. [CrossRef] [PubMed]

36. Erge, O.; van Oort, E. Time-dependent cuttings transport modeling considering the effects of eccentricity, rotation and partial blockage in wellbore annuli. *J. Nat. Gas Sci. Eng.* **2020**, *82*, 103488. [CrossRef]
37. Erge, O.; van Oort, E. Modeling the effects of drillstring eccentricity, pipe rotation and annular blockage on cuttings transport in deviated wells. *J. Nat. Gas Sci. Eng.* **2020**, *79*, 103221. [CrossRef]
38. El Tani, M. Circular Tunnel in a Semi-Infinite Aquifer. *Tunn. Undergr. Space Technol.* **2003**, *18*, 49–55. [CrossRef]
39. Gattinoni, P.; Scesi, L. An Empirical Equation for Tunnel Inflow Assessment: Application to Sedimentary Rock Masses. *Hydrogeol. J.* **2010**, *18*, 1797–1810. [CrossRef]
40. Zhang, X.; Wang, M.; Feng, D.; Wang, J. Water inflow amount prediction for karst tunnel with steady seepage conditions. *Sustainability* **2023**, *15*, 10638. [CrossRef]
41. Tian, L.; Zhang, Q.; Li, X.; Li, C. Fracturing Effectiveness Evaluation Based on Flowback Data Using Pressure Transient Testing. *Reserv. Sci.* **2026**, *2*, 97–110. [CrossRef]
42. Ali, J.; Ansari, U.; Ali, F.; Javed, T.; Hullio, I.A. Application of Machine Learning for Effective Screening of Enhanced Oil Recovery Methods. *Reserv. Sci.* **2026**, *2*, 65–80. [CrossRef]

Disclaimer/Publisher's Note: The statements, opinions and data contained in all publications are solely those of the individual author(s) and contributor(s) and not of MDPI and/or the editor(s). MDPI and/or the editor(s) disclaim responsibility for any injury to people or property resulting from any ideas, methods, instructions or products referred to in the content.